Materials Transactions, Vol. 62, No. 3 (2021) pp. 403 to 411

Silicon Refining by Solidification from Liquid Si–Zn Alloy and Floating Zone Method

Yuanjia Ma[1,*1], Kouji Yasuda[2,3,*2], Akifumi Ido[2,*3], Takeyuki Shimao[2,*4], Ming Zhong[1,*5], Rika Hagiwara[2] and Toshiyuki Nohira[1,*6]

[1]*Institute of Advanced Energy, Kyoto University, Uji 611-0011, Japan*
[2]*Graduate School of Energy Science, Kyoto University, Kyoto 606-8501, Japan*
[3]*Agency for Health, Safety and Environment, Kyoto University, Kyoto 606-8501, Japan*

This study evaluated the refining ability of a proposed production process for solar-grade silicon utilizing the electrolytic reduction of SiO_2 on a liquid zinc electrode in molten salt. The distribution behaviors of impurity elements during the precipitation of solid silicon from a liquid Si–Zn alloy were studied by thermodynamic calculations at 923 K. In the precipitation experiment, silicon granules were recovered from a liquid Si–Zn alloy, which was prepared from metallurgical-grade silicon. The impurity removal ratios exceeded 99% for C, Al, and Ca, and 90% for Fe. High removal ratios were attained for B and O as well. As the post-processing, a silicon ingot was produced from the precipitated silicon granules by the floating zone method. The Zn residue in the precipitated silicon was completely evaporated during the floating zone refining. The total content of metallic elements (Al, Ca, Fe, Ti, and Zn) was lower than 0.2 ppmw, even though metallurgical-grade silicon was used as the starting material. [doi:10.2320/matertrans.M-M2020872]

(Received June 27, 2020; Accepted December 4, 2020; Published February 5, 2021)

Keywords: *solar-grade silicon, silicon purification, liquid alloy, molten salt*

1. Introduction

Photovoltaic (PV) power generation has attracted considerable attention as a clean and inexhaustible energy, which is expected to be a key technology to mitigate energy and environmental issues. Although PV power only accounted for 1.7% of the worldwide energy supply in 2017, according to World Energy Outlook 2018 by the International Energy Agency (IEA),[1)] it is expected to increase to 10% by 2040 if the cost of PV cell production is reduced.[2)] The global production of PV cells achieved 102.4 GW in 2018, approximately 350 times the value in 2000.[3)] Among the many types of solar cells, crystalline silicon solar cells accounted for 96.9% of the worldwide production in 2018.[4)] The global production of high-purity crystalline silicon also increased to 448,000 tons in 2018, by a factor of approximately 20 compared to that in 2000.[5)] Consequently, crystalline silicon solar cells are expected to remain mainstream in the PV industry in the long term.

High-purity silicon used in crystalline silicon solar cells is known as solar-grade silicon (SOG-Si), which requires a purity of 6–7 N. Currently, SOG-Si is produced by the following steps: (1) production of metallurgical-grade silicon (MG-Si) from SiO_2 by carbothermal reduction, (2) production and purification of trichlorosilane, and (3) production of polycrystalline silicon from trichlorosilane gas by chemical vapor deposition (CVD).[6–8)] Steps (2) and (3) are referred to as the Siemens process. Although the purity of silicon produced by the Siemens process is very high, low productivity and high energy consumption hinder cost reduction. To develop a next-generation production process for SOG-Si, purification of MG-Si[9–13)] and metallothermic reduction of silicon halides by metal reductants[14–17)] have been investigated.

Over the past two decades, we have been studying the electrolytic reduction of SiO_2 to silicon in molten $CaCl_2$ to develop a new production process for SOG-Si.[18–22)] In molten $CaCl_2$, electrochemical reduction of insulating SiO_2 is realized by using a SiO_2 contacting electrode, which provides the three-phase zone of conductor/SiO_2/$CaCl_2$. The produced silicon, which has high electrical conductivity at high temperature, becomes an additional electron pathway.

$$SiO_2(s) + 4\ e^- \rightarrow Si(s) + 2\ O^{2-} \quad (1)$$

Several other research groups have also investigated the direct electrolytic reduction of SiO_2.[23–33)]

With the aim of efficient recovery of reduced silicon, we also proposed an electrolytic reduction process of SiO_2 using a liquid zinc cathode in molten $CaCl_2$.[34–36)] Figure 1 schematically illustrates the proposed process.[35,36)] The overall process consists of three major steps: electrolysis, precipitation, and refining. In the electrolysis step, solid SiO_2 is reduced to form a Si–Zn liquid alloy at the cathode. The separation of reduced silicon from the molten salt is simple because the reduced silicon forms a liquid Si–Zn alloy at the cathode.

$$SiO_2(s) + \text{Si–Zn}(l, \text{low Si conc.}) + 4\ e^- \rightarrow \text{Si–Zn}(l, \text{high Si conc.}) + 2\ O^{2-} \quad (2)$$

In the precipitation step, solid silicon is precipitated by decreasing the temperature of the liquid Si–Zn alloy.

$$\text{Si–Zn}(l, \text{high Si conc.}) \rightarrow Si(s) + \text{Si–Zn}(l, \text{low Si conc.}) \quad (3)$$

The liquid Si–Zn alloy with a low concentration of Si is reused as the cathode in the electrolysis step. The recovered

*[1]Graduate Student, Kyoto University
*[2]Present address: Graduate School of Engineering, Kyoto University, Kyoto 606-8501, Japan
*[3]Graduate Student, Kyoto University, Present address: Central Research Institute of Electric Power Industry, Yokosuka 240-0196, Japan
*[4]Graduate Student, Kyoto University, Present address: Panasonic Corp., Kaizuka 597-0094, Japan
*[5]Present address: School of Metallurgy, Northeastern University, Shenyang 110819, China
*[6]Corresponding author, E-mail: nohira.toshiyuki.8r@kyoto-u.ac.jp

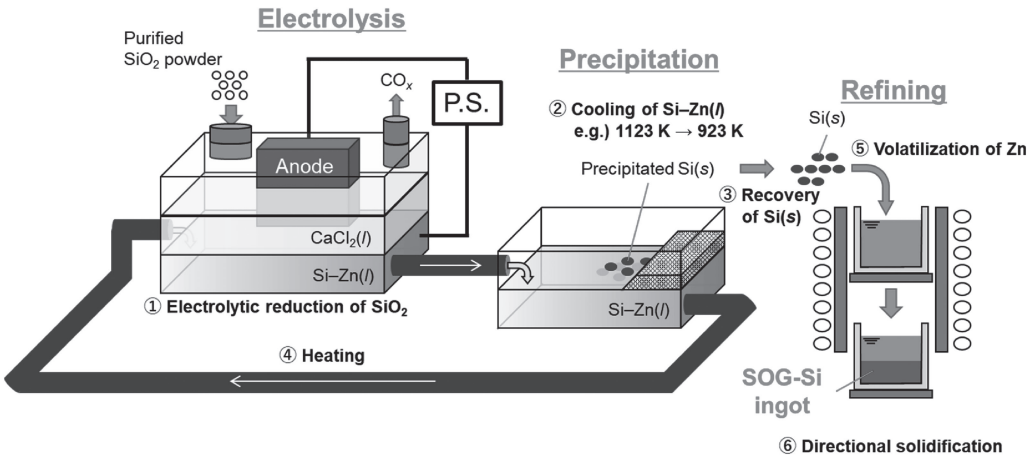

Fig. 1 A schematic drawing of the SOG-Si production process using electrochemical reduction of SiO_2 powder on a liquid Si–Zn alloy cathode in molten $CaCl_2$.[35,36]

silicon is then subjected to a refining step that comprises vacuum refining to remove residual Zn and directional solidification to manufacture SOG-Si ingots.

Silicon refining by solidification has been widely investigated not only for liquid silicon, but also for liquid Si–Al alloys,[37–40] Si–Cu alloys,[41] Si–Sn alloys,[42] and Si–Fe alloys.[43,44] Although the refining of silicon using a liquid Si–Zn alloy is also considered to be possible, there are no reports so far, likely due to the experimental difficulty caused by the high vapor pressure of Zn. In our previous study,[36] silicon granules were obtained by the electrolysis of SiO_2 particles on a zinc cathode in molten $CaCl_2$, and the concentrations of impurity elements (B, P, Al, Ca, Fe, Ti, and Zn) in the silicon granules were analyzed. However, the impurity behaviors during the precipitation and refining steps have not been quantitatively investigated. Through the previous experiment, we realized that the evaporation of zinc can be largely suppressed, even at 1123 K, the electrolysis temperature of SiO_2, by submerging the Si–Zn alloy in molten $CaCl_2$.[35] The lower evaporation rate is explained by the low solubility of zinc in the molten salt. This method enables the distribution analysis of impurities during the refining of silicon by solidification from a liquid Si–Zn alloy.

In the present study, the distribution coefficients of impurity elements between solid Si and liquid Zn were calculated from thermodynamic data at the precipitation temperature of 923 K. Then, the behaviors of impurity elements in the precipitation step were experimentally evaluated using the liquid Si–Zn alloy, which was prepared from low-purity MG-Si. Finally, the precipitated silicon was melted and refined using the floating zone (FZ) method to analyze the behavior of impurities in the refining step.

2. Experimental

2.1 Silicon refining by solidification from liquid Si–Zn alloy

Figure 2 shows a schematic drawing of the experimental apparatus for the precipitation of solid silicon from a liquid Si–Zn alloy. 885 g of metallic zinc (FUJIFILM Wako Pure Chemical Corp., reagent grade, granule) and 197 g of $CaCl_2$ (Kojundo Chemical Laboratory Co., Ltd., >99%) were

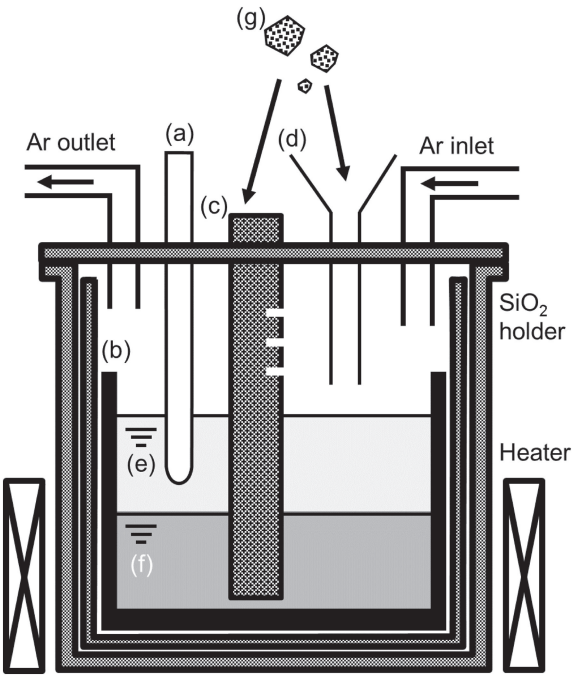

Fig. 2 A schematic drawing of the experimental apparatus for the precipitation of solid silicon from a liquid Si–Zn alloy. (a) Thermocouple, (b) graphite crucible, (c) carbon tube (Exp. (1)), (d) funnel (Exp. (2)), (e) molten $CaCl_2$, (f) liquid zinc, and (g) MG-Si.

charged in a graphite crucible (Toyo Tanso Co., Ltd., IG-110 grade, o.d. 80 mm × i.d. 70 mm × height 200 mm) and dried under vacuum at 773 K overnight. The evaporation of metallic zinc was suppressed by submerging the Si–Zn alloy in molten $CaCl_2$. After the temperature was increased to 1123 K in a dry argon atmosphere, 20.0 g of MG-Si, which is equivalent to 5.0 at% of the prepared Si–Zn alloy, was charged through a carbon tube (Experiment 1) or a glass funnel (Experiment 2). The carbon tube had several holes cut at the face of the tube side to maintain both bath level and gas pressure equalization between the inside and outside of the tube. After the temperature was maintained at 1123 K for more than 24 h to sufficiently react with the silicon and zinc, the liquid Si–Zn alloy was cooled. Figure 3 shows the temperature changes during the cooling steps. In Experi-

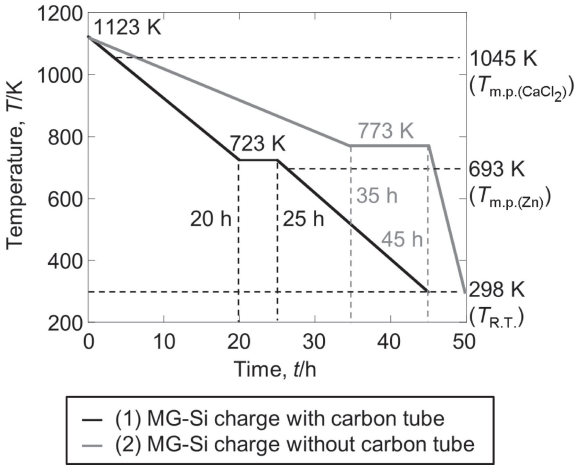

Fig. 3 Temperature changes during the cooling step.

ment 1, the temperature was decreased from 1123 K to 723 K for 20 h, then maintained at 723 K for 5 h, and further reduced to 298 K for 20 h. In Experiment 2, the temperature was decreased from 1123 K to 773 K for 35 h, then maintained at 773 K for 10 h, and further decreased to 298 K for 5 h. A lump of zinc metal was recovered from the crucible after dissolution of $CaCl_2$ with distilled water. The zinc metal lump was dissolved in a hydrochloric acid solution (20 mass%) to recover the precipitated silicon granules. The recovered silicon granules were then immersed in a hydrochloric acid solution (10 mass%) overnight.

2.2 Silicon refinement and zinc evaporation by the FZ method

A portion of the silicon granules recovered in the precipitation experiment (Experiment 2) was crushed into powder in an agate mortar. Silicon powder with sizes below 0.1 mm was selected by a sieve and molded into a cylinder with a diameter of approximately 7 mm by isostatic pressing under a pressure of 60 MPa for 1 min. The molded silicon cylinder was hung with a platinum wire and inserted into a quartz tube of a floating zone furnace (Canon Machinery Inc., Desktop type A) as a feed silicon, as shown in Fig. 4. A 10N-purity poly-silicon rod (Furuuchi Chemical Corp., diameter 5 mm) was used as the seed silicon. The zone melting was conducted twice to evaporate the residual Zn to obtain a silicon ingot in an inverse argon stream with a uniform speed of 20–30 mm h^{-1} and a lamp voltage of 55–65 V. Silicon wafers were cut out from the prepared silicon ingot using a diamond wheel saw (South Bay Technology Inc., SBT650).

2.3 Impurity analysis of silicon samples

The analyses of impurity elements in the silicon samples were conducted using the high-frequency combustion–infrared absorption method (LECO, CS-LS600) for carbon analysis, inert gas fusion–infrared absorption method (LECO, TC600) for oxygen analysis, and glow discharge mass spectrometry (GD-MS; VG Elemental, VG 9000) for the other elements. Silicon samples were immersed in a hydrofluoric acid solution (20–25 mass%) for 20 min and then washed with distilled water and acetone before GD-MS analysis.

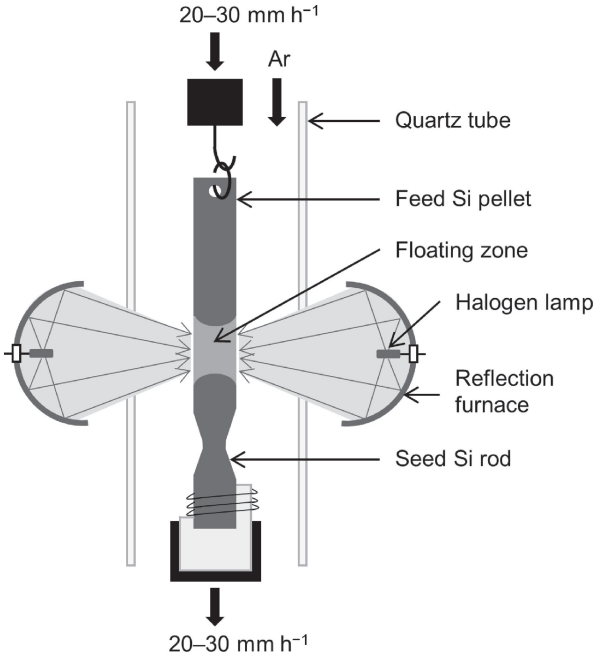

Fig. 4 A schematic drawing of the floating zone (FZ) method.

3. Thermodynamic Calculations

In order to predict the purification ability of the precipitation step, the distribution behaviors of the impurity elements were evaluated. When the temperature was decreased to 923 K from the electrolysis temperature of 1123 K, solid silicon corresponding to 5 at% was recovered. Although the liquid Zn equilibrated with solid Si at 923 K contains 1 at% Si, the distribution behavior of impurities was evaluated assuming that the liquid Zn contained no Si. That is, the distribution coefficients of impurities between solid Si and liquid Zn were calculated at infinite dilution.

When the standard state of impurity element A is defined as its pure stable state at 923 K, the activities of A in an equilibrium state are identical in both phases.

$$a_{A(Zn(l))} = a_{A(Si(s))} \tag{4}$$

The activity is the product of activity coefficient and mole fraction as follows:

$$\gamma_{A(Zn(l))} x_{A(Zn(l))} = \gamma_{A(Si(s))} x_{A(Si(s))} \tag{5}$$

Here, $\gamma_{A(Zn(l))}$ and $\gamma_{A(Si(s))}$ are the activity coefficients, and $x_{A(Zn(l))}$ and $x_{A(Si(s))}$ are the mole fractions of A in liquid Zn and solid Si, respectively. The activity coefficient, γ_A, is identical to the activity coefficient at infinite dilution, γ°_A, when the concentration is low enough and the Henry's law can be applied. Thus, the distribution coefficient of A at infinite dilution, k°_A, is defined as the ratio of the mole fraction of solid Si phase to the liquid Zn phase as follows:

$$k^\circ_A = \frac{x_{A(Si(s))}}{x_{A(Zn(l))}} \tag{6}$$

$$= \frac{\gamma^\circ_{A(Zn(l))}}{\gamma^\circ_{A(Si(s))}} \tag{7}$$

where, $\gamma^\circ_{A(Zn(l))}$ and $\gamma^\circ_{A(Si(s))}$ are the activity coefficients of A at infinite dilution in liquid Zn and solid Si, respectively.

Table 1 Equilibrated phases with saturated solid Si or liquid Zn at 923 K and their standard Gibbs energy of formation at 923 K.

Impurity element, A	Equilibrated phase at 923 K / Standard Gibbs energy of formation at 923 K, ΔG°_f (kJ mol^{-1})	
	Solid Si	Liquid Zn
B	SiB_3 (*s*) / — [a]	B (*s*) / 0
C	SiC (*s*) / −65.920 [50]	C (*s*) / 0
O	SiO_2 (*s*) / −743.753 [50]	ZnO (*s*) / −255.998 [51,52]
P	SiP (*s*) / −38.843 [51,53,54]	Zn_3P_2 (*s*) / −83.504 [51,55]
Al	Al–Si (*l*) / — [a]	— [b] / — [a]
Ca	$CaSi_2$ (*s*) / −123.916 [53,54,56]	$CaZn_{13}$ (*s*) / −108.861 [57–61]
Fe	$FeSi_2$ (*s*) / −70.483 [62]	$FeZn_7$ (*s*) / −12.030 [63]
Ti	$TiSi_2$ (*s*) / −164.702 [53,64]	$TiZn_3$ (*s*) / −57.604 [65]

a: The data were not used to calculate the activity coefficient at infinite dilution because the reported coefficient was used in this study

b: Liquid Al–Zn alloy has a wide composition range

Although the equilibrium expressed in eq. (4) is attained for the A–Zn–Si ternary system, the value of $\gamma^\circ_{A(Zn(l))}$ and $\gamma^\circ_{A(Si(s))}$ can be calculated from A–Zn and A–Si binary systems with the assumption that interaction between impurity and Zn in solid Si and that between impurity and Si in liquid Zn can be ignored.

Typical impurity elements of B, C, O, P, Al, Ca, Fe, and Ti were selected for the present evaluation. Since the temperature dependences of γ°_A have been already reported for B–Si,[45] Al–Si,[46] and Al–Zn[47] binary systems, the values at 923 K were calculated based on these reports. For other systems, γ°_A was evaluated from the phase diagrams and thermodynamic data. Table 1 summarizes the equilibrated phases with saturated solid Si or liquid Zn at 923 K, which are given by the binary phase diagrams for the A–Si and A–Zn systems.[48,49] Furthermore, their standard Gibbs energy of formation, ΔG°_f, at 923 K is also given in Table 1.[50–65]

For some cases, the equilibrium between solid Si and compound A_ySi_z is considered, where y and z are the stoichiometry of the compound. In an equilibrium state, the activities of A in the Si phase, $a_{A(Si(s,\,sat))}$, and in the A_ySi_z phase, $a_{A(A_ySi_z)}$, are identical. The same is applicable to the activities of silicon $a_{Si(Si(s,\,sat))}$ and $a_{Si(A_ySi_z)}$.

$$a_{A(Si(s,\,sat))} = a_{A(A_ySi_z)} \tag{8}$$

$$a_{Si(Si(s,\,sat))} = a_{Si(A_ySi_z)} \tag{9}$$

The Gibbs energy of formation of A_ySi_z, $\Delta G^\circ_f(A_ySi_z)$, is given by the following equation:

$$\Delta G^\circ_f(A_ySi_z) = RT\ln\left(\frac{a^y_{A(A_ySi_z)}a^z_{Si(A_ySi_z)}}{a_{A_ySi_z(A_ySi_z)}}\right) \tag{10}$$

Here, R is the gas constant (8.3145 J mol^{-1} K^{-1}), T is the absolute temperature, and $a_{A_ySi_z(A_ySi_z)}$ is the activity of A_ySi_z in the A_ySi_z compound. Here, the standard state of A_ySi_z is its pure stable state at 923 K. If there is no solubility of A_ySi_z in other phases, $a_{A_ySi_z(A_ySi_z)}$ is regarded as unity.

$$a_{A_ySi_z(A_ySi_z)} = 1 \tag{11}$$

The activity of Si in the solid Si phase is also regarded as unity because the amount of impurities in the Si phase is very small.

$$a_{Si(Si(s,\,sat))} = 1 \tag{12}$$

From these equations, the activity of A in the solid silicon phase is obtained from the following equation:

$$a_{A(Si(s,\,sat))} = \exp\left(\frac{\Delta G^\circ_f(A_ySi_z)}{yRT}\right) \tag{13}$$

Then, $\gamma^\circ_{A(Si(s))}$ is calculated from the solubility of A in the solid Si phase, $x_{A(Si(s,\,sat))}$, as follows:

$$\gamma^\circ_{A(Si(s))} = \frac{a_{A(Si(s,\,sat))}}{x_{A(Si(s,\,sat))}} \tag{14}$$

$$= \frac{\exp\left(\frac{\Delta G^\circ_f(A_ySi_z)}{yRT}\right)}{x_{A(Si(s,\,sat))}} \tag{15}$$

In a similar manner, $\gamma^\circ_{A(Zn(l))}$ is obtained by replacing Si(s) with Zn(l) in the above discussion. Here, the activity of Zn in the Zn(l) phase, $a_{Zn(Zn(l,\,sat))}$, needs further consideration. As shown in the phase diagrams, the solubility of impurities in the liquid Zn phase can reach several atomic percent at 923 K. Therefore, the value of $a_{Zn(Zn(l,\,sat))}$ cannot be regarded as unity where the standard state is pure liquid Zn, but rather regarded as the mole fraction of Zn, $x_{Zn(Zn(l,\,sat))}$, assuming Raoult's law.

$$a_{Zn(Zn(l,\,sat))} = x_{Zn(Zn(l,\,sat))} \tag{16}$$

$$a_{Zn(A_yZn_z)} = a_{Zn(Zn(l,\,sat))} = 1 - x_{A(Zn(l,\,sat))} \tag{17}$$

Consequently, the value of $\gamma^\circ_{A(Zn(l))}$ is obtained as follows:

$$a_{A(Zn(l,\,sat))} = (1 - x_{A(Zn(l,\,sat))})^{-\frac{z}{y}}\exp\left(\frac{\Delta G^\circ_f(A_yZn_z)}{yRT}\right) \tag{18}$$

$$\gamma^\circ_{A(Zn(l))} = \frac{(1 - x_{A(Zn(l,\,sat))})^{-\frac{z}{y}}\exp\left(\frac{\Delta G^\circ_f(A_yZn_z)}{yRT}\right)}{x_{A(Zn(l,\,sat))}} \tag{19}$$

Table 2 summarizes the solubilities of the impurity elements in solid Si and liquid Zn phases at 923 K.[46,48,51,60,66–76] The solubilities of P(Zn(l)), Al(Zn(l)), Ca(Zn(l)), Fe(Zn(l)), and Ti(Zn(l)) were read from the phase diagrams.[48,76] Most of the other solubility values were calculated from the reported functions of solubility with regards to temperature.[46,48,51,60,66–76] As for B(Zn(l)), the solubility was calculated from the interaction parameter of liquid B–Zn under the assumption of regular solution model, $\Omega_{B,Zn}$, 2.98×10^4 J mol^{-1} at 923 K, reported by Chen *et al.*[68] In this calculation, the standard state of B is not a pure solid B, which is the stable phase at 923 K, but pure liquid B. When solid B and B-saturated liquid B–Zn are in an equilibrium state, the activity of B in liquid B–Zn with liquid B as the standard state, $a_{B(l,\,Zn(l,\,sat))}$, is expressed by the Gibbs energy of fusion of B, ΔG_{fus}(B).

$$\ln\left(\frac{a_{B(l,\,Zn(l,\,sat))}}{a_{B(l)}}\right) = -\frac{\Delta G_{fus}(B)}{RT} \tag{20}$$

Since its standard state is pure liquid ($a_{B(l)} = 1$),

Table 2 Solubility of each impurity element in solid Si and liquid Zn at 923 K.

Impurity element, A	Solubility			
	In solid Si, $x_{A(Si(s,\,sat))}$	Ref. number	In liquid Zn, $x_{A(Zn(l,\,sat))}$	Ref. number
B	2.0×10^{-4} [a]	66)	4.7×10^{-4}	51, 60, 67, 68)
C	2.2×10^{-11} [a]	69)	2.3×10^{-5} [a]	46)
O	1.2×10^{-6} [a]	70)	3.6×10^{-4}	71)
P	3.8×10^{-3} [a]	72)	1.0×10^{-2}	48)
Al	5.0×10^{-5} [a]	46)	0.97	48)
Ca	6.5×10^{-6} [a]	73)	3.0×10^{-2}	48)
Fe	3.2×10^{-13} [a]	74)	2.0×10^{-2}	48)
Ti	4.7×10^{-17} [a]	75)	5.0×10^{-3}	76)

a: Extrapolated values

Table 3 Activity coefficient of each impurity element at infinite dilution in solid Si and liquid Zn with the standard states of their stable phase and distribution coefficient between solid Si and liquid Zn at 923 K.

Impurity element, A	Activity coefficient at infinite dilution		Distribution coefficient, $k^{\circ}{}_{A}$ *
	In solid Si, $\gamma^{\circ}{}_{A(Si(s))}$	In liquid Zn, $\gamma^{\circ}{}_{A(Zn(l))}$	
B	1.4×10^{4} 45)	2.1×10^{3}	1.5×10^{-1}
C	8.6×10^{6}	4.4×10^{4}	5.1×10^{-3}
O	7.8×10^{-16}	9.2×10^{-12}	1.2×10^{4}
P	1.7	4.4×10^{-1}	2.6×10^{-1}
Al	3.3×10^{4} 46)	2.6 47)	7.9×10^{-5}
Ca	1.5×10^{-2}	3.4×10^{-5}	2.3×10^{-3}
Fe	3.3×10^{8}	1.2×10	3.6×10^{-8}
Ti	4.6×10^{7}	1.1×10^{-1}	2.4×10^{-9}

*: $k^{\circ}{}_{A} = \gamma^{\circ}{}_{A(Zn(l))} / \gamma^{\circ}{}_{A(Si(s))}$

$$\ln a_{B(l,\,Zn(l,\,sat))} = -\frac{\Delta G_{fus}(B)}{RT} \tag{21}$$

is given. Then, $a_{B(l,\,Zn(l,\,sat))}$ is calculated to be 2.29×10^{-2} at 923 K from the reported $\Delta G_{fus}(B)$ value of 2.90×10^{4} J mol^{-1}.[51,60,61] In the equilibrium state, the following equation holds.

$$RT\ln a_{B(l,\,Zn(l,\,sat))} = \Omega_{B,Zn}(1-x_{B(Zn(l,\,sat))})^{2} + RT\ln x_{B(Zn(l,\,sat))} \tag{22}$$

By substituting $a_{B(l,\,Zn(l,\,sat))} = 2.29\times10^{-2}$ and $\Omega_{B,Zn} = 2.98\times10^{4}$, the value of $x_{B(Zn(l,\,sat))}$ was calculated to be 4.7×10^{-4}.

The calculated activity coefficients of impurity elements at infinite dilution in solid Si and liquid Zn are summarized in Table 3. Then, the distribution coefficients can be calculated using eq. (4), which are also listed in Table 3. The distribution coefficient of O (1.2×10^{4}) is substantially large, indicating that almost all the O impurity in the liquid Si–Zn alloy transfers to solid Si. On the other hand, the distribution coefficients of C, Al, Ca, Fe, and Ti are 5.1×10^{-3}, 7.9×10^{-5}, 2.3×10^{-3}, 3.6×10^{-8}, and 2.4×10^{-9}, respectively. Thus, these impurities are considered to remain in the liquid Si–Zn alloy during the precipitation step. The removal of B and P is known to be difficult in simple solidification refining from liquid Si because of the large distribution coefficients, that is, 0.8 for B and 0.35 for P.[77] In the present calculation, the distribution coefficients are 0.15 for B and 0.26 for P. The obtained smaller values compared to those for the Si(s)/Si(l) system demonstrate that the effective removal of B and P is possible by utilizing the liquid Si–Zn alloy system. All of these calculations indicate that the electrolytic process using a liquid Si–Zn alloy as a cathode has the advantages of high refining ability and high resistance against impurity inclusion. Even when carbon is deposited onto the cathode by the reduction of CO_3^{2-} ions produced at a carbon anode, it is not contained in the solid Si phase in the precipitation step. The applicability of graphite anodes in the electrolysis step is a significant advantage for practical applications.

For reference, the distribution coefficients of B for the liquid Si–Al alloy were reported to be 0.49 at 1473 K and 0.22 at 1273 K,[45] and those of P were 0.12 at 1373 K and 0.061 at 1173 K.[78] The distribution coefficients of both elements become smaller at lower temperatures. Although 923 K is even lower than the cases of the liquid Si–Al alloy, the distribution coefficients of the liquid Si–Zn alloy, 0.15 for B, and 0.26 for P, are higher than those for the Si–Al alloy. This is explained by the fact that the affinity of Zn to these impurities is lower than that of Al.

4. Results and Discussion

4.1 Silicon refining by solidification from liquid Si–Zn alloy and the FZ method

Figure 5(a) shows an optical image of the top view of the zinc ingot obtained from the precipitation experiment (1). The top portion consists of a metallic colored main body and gray–blue parts. Although the bottom part cannot be seen from the figure, the entire bottom was a metallic color. Figure 5(b) shows a cross-sectional SEM image of the zinc ingot. The top portion contains many 100–1000-μm particles. From EDX analysis, only Si was detected for the deposited particles, while only Zn was detected in the main body. Most deposited particles were observed at the top of the ingot, and a small amount of silicon particles were also found at the edge of the middle part of the lump. Considering the densities of liquid Zn, $\rho_{Zn(l)} = 6.56\,g\,cm^{-3}$,[79] and solid Si, $\rho_{Si(s)} = 2.32\,g\,cm^{-3}$,[80] at 723 K, silicon particles floated at the top of the liquid zinc during the precipitation step. Figure 5(c) shows an optical image of the silicon granules recovered after acid leaching of the zinc lump. The granules have a size of approximately 1 mm and exhibit a metallic luster.

Figure 6 shows a cross-sectional SEM image of the zinc ingot obtained from the precipitation experiment (2). Similar to the zinc ingot obtained from experiment (1), many Si particles were deposited in the upper part. On the other hand, the image shows much larger size particles of 300–2000 μm and more inclusion of zinc into the gaps of silicon granules, compared with experiment (1). This result is attributed to

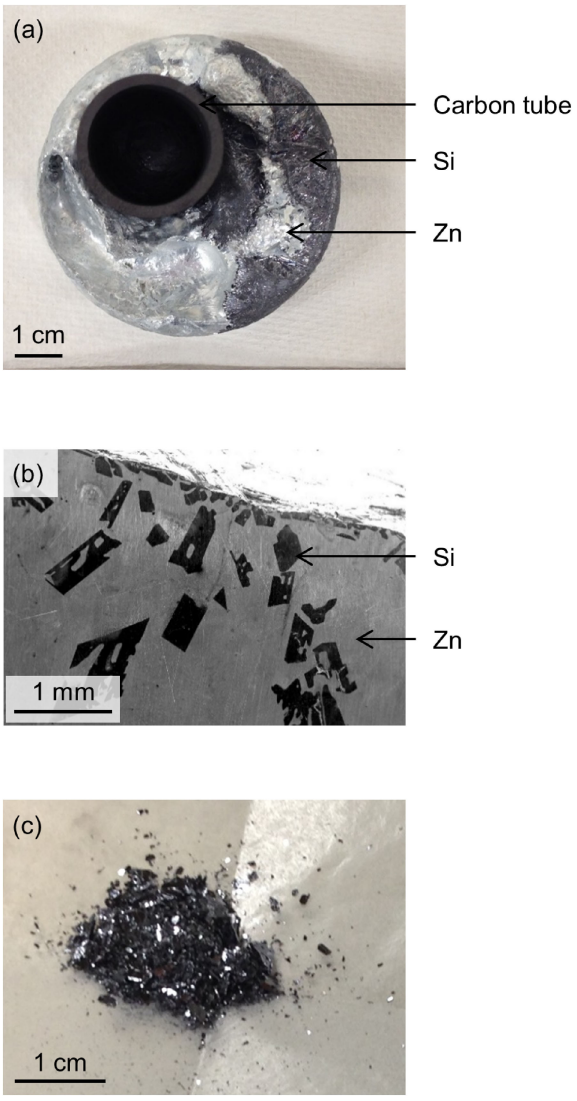

Fig. 5 (a) An optical image of a top view and (b) a SEM image of a cross section of the zinc ingot obtained after the precipitation experiment (1) in molten $CaCl_2$, and (c) an optical image of the silicon granules recovered after acid leaching of the zinc ingot.

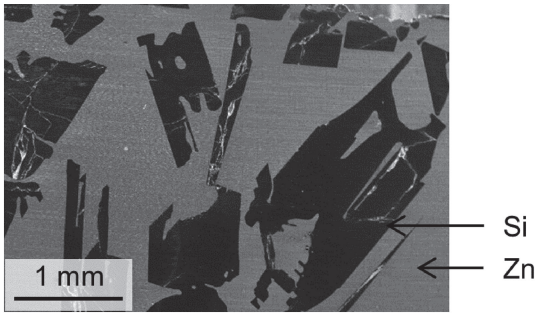

Fig. 6 A SEM image of a cross section of the zinc ingot obtained after the precipitation experiment (2) in molten $CaCl_2$.

the progressive crystal growth of silicon particles during precipitation at a lower cooling rate (experiment (1): $20\,K\,h^{-1}$, (2): $10\,K\,h^{-1}$).

Figure 7(a) shows an optical image of the silicon powder obtained by crushing the silicon granules prepared in the precipitation experiment (2). From this silicon powder, a

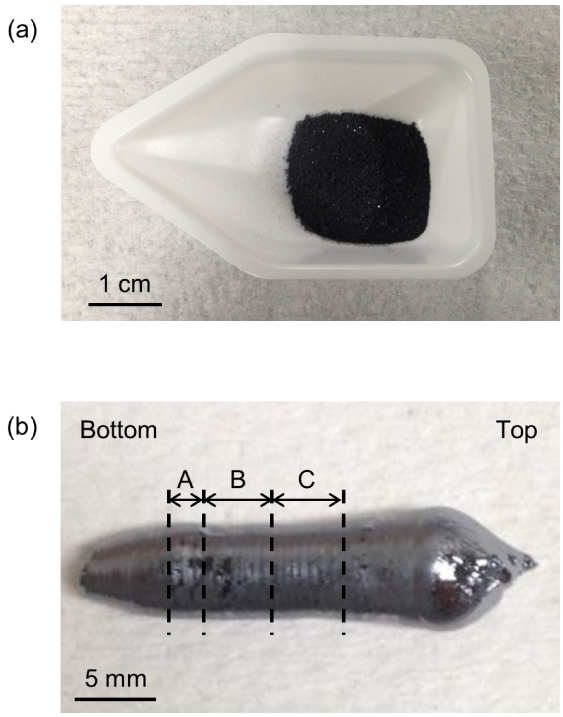

Fig. 7 Optical images of (a) silicon powder for silicon ingot and (b) silicon ingot obtained by FZ melting.

silicon ingot was obtained by FZ melting, as shown in Fig. 7(b). The ingot has a gray–blue metallic luster and a diameter of 3–5 mm and length of 25 mm. The non-uniform patterns observed on the surface suggest that the silicon ingot is polycrystalline. In general, the crystallinity can be improved by slowing the moving speed during FZ melting. The ingot was cut with a diamond wheel saw at the broken lines indicated in Fig. 7(b). The sliced wafers were used to analyze the impurity contents. Specifically, parts A, B, and C were used for GD-MS analysis, carbon analysis, and oxygen analysis, respectively.

4.2 Impurity analysis of silicon samples

Table 4 lists the impurity contents in the silicon granules obtained in the precipitation experiments (1) and (2) and the silicon wafers obtained by FZ melting. The values for the original MG-Si are also listed for reference. The removal fractions in the precipitation experiments, r_A, which are calculated from the contents in the original MG-Si, $x_{A(MG\text{-}Si)}$, and the precipitated silicon, $x_{A(prec\ Si)}$, are shown in parentheses.

$$r_A = \left(1 - \frac{x_{A(prec\ Si)}}{x_{A(MG\text{-}Si)}}\right) \times 100 \qquad (23)$$

For the precipitated silicon granules, the removal fractions of Al, Ca, and Ti exceeded 99%, and the fractions of B, C, and Fe exceeded 90%. The high removal fractions agree with the low distribution coefficients calculated in Section 3. It is noteworthy that the removal fraction of B was above 95%. The removal of B is known to be difficult in the solidification refining from liquid silicon because the distribution coefficient between Si(s)/Si(l) is as high as 0.8.[77] The removal of P has also been achieved at fractions

Table 4 Impurity contents in silicon samples with removal fractions and acceptable impurity levels for SOG-Si.

Impurity element A	Impurity content in Si *, x_A / ppmw (Removal fraction †, r_A)				Acceptable level for SOG-Si, $x_{A(SOG)}$ / ppmw
	MG-Si	Precipitated Si		Si wafer after FZ melting	
		(1)	(2)		
B	11	0.6 (94.9%)	0.55 (95.0%)	1.9	0.1–0.3
P	96	32 (66.7%)	44 (54.2%)	13	0.03–0.14
O	400 [a]	77 (80.8%)	40 [a] (90.0%)	10 [a]	— [c]
C	2300 [b]	87 (96.2%)	20 [b] (99.1%)	50 [b]	<10
Al	770	<0.5 (>99.9%)	**0.07** (>99.9%)	**0.05**	<0.1
Ca	210	<0.5 (>99.8%)	**0.11** (99.9%)	**<0.01**	<0.2
Fe	1900	13 (99.3%)	53 (97.2%)	0.11	<0.1
Ti	150	<0.1 (>99.9%)	0.74 (99.5%)	<0.01	$<10^{-3}$
Zn	<1	310	5900	<0.01	— [c]

*: Analyzed by GD-MS
†: $r_A = (1-x_{A(\text{prec Si})} / x_{A(\text{MG-Si})}) \times 100$
a: Analyzed by IR after inert gas fusion method
b: Analyzed by IR after combustion method
c: No data

of 54.2% and 66.7%. However, the removal fractions are smaller than expected, which might be due to the formation of a $ZnSiP_2$ compound with a melting point of 1643 K.[81,82] Concerning the removal fraction of O, high values of 80.8% and 90.0% were obtained, which is inconsistent with the calculated distribution coefficient of 1.2×10^4. As the concentration of O in MG-Si is obviously higher than the solubility limit in the solid Si phase,[83] the presence of some oxides, except for SiO_2, such as CaO, in MG-Si is indicated. Thus, the dissolution of oxides into molten $CaCl_2$ contributed to the removal of O.

Comparing the impurity contents in the silicon granules obtained from the precipitation experiments (1) and (2), larger amount of Zn was detected in experiment (2). This is explained by the larger amount of Zn left in the gaps of the granules, as observed in the cross-sectional SEM image. For other impurity elements, no significant difference was found. Summarizing the above, high processing rate and small inclusion of zinc can be achieved at a high cooling rate. On the other hand, large silicon granules are obtained at a low cooling rate, which will be advantageous for silicon recovery from liquid Si–Zn alloy by filtering.

For the silicon wafer obtained by FZ melting, metal elements (Al, Ca, Fe, Ti, and Zn) were further removed from the precipitated silicon granules; the total concentration was less than 0.2 ppmw. It should be mentioned that Zn was effectively removed to less than 0.01 ppmw owing to its high vapor pressure,[84] even though a relatively large amount of 5900 ppmw remained in the silicon granules. In this respect, this contrasts with the previous solidification refining from Si–M (M = Al, Cu, Fe, Sn, etc.) alloys. The residue of the alloying element in silicon is known as one of the major challenges of solidification refining. For the solidification refining from the Si–Al alloy, approximately 400–600 ppmw of Al remained in the precipitated silicon.[85] As the distribution coefficient of Al in Si is 2×10^{-3},[86] at least twice the directional solidification refining is required for Al removal. Thus, the extremely easy removal of Zn is considered to be a great advantage as an alloying element. In the silicon wafer, P and O were also further removed to 13 ppmw and 10 ppmw, respectively. In contrast, B and C increased compared with the precipitated silicon granules, perhaps because carbon is considered to be contaminated by a diamond wheel saw. The increase in B needs further study.

Compared with the acceptable level for SOG-Si shown in Table 4, the contents of Al and Ca in the silicon wafer meet the level in spite of their high contents in MG-Si. It is noteworthy that the concentration of O is lower than that in actual silicon wafers used for solar cells, that is, approximately 20 ppmw,[83] which is produced by the CZ method. Although the contents of Fe, Ti, B, and P are higher than the acceptable level, this is mainly due to the high impurity contents in the starting material of MG-Si. When electrochemically reduced silicon, which has lower impurity contents than MG-Si, is used as the starting material, lower concentrations of Fe, Ti, B, and P are expected to be achieved.

5. Conclusion

The distribution behaviors of impurity elements between solid Si and liquid Zn were studied by thermodynamic calculations and experiments. The distribution coefficients of impurity elements were calculated from the reported data at 923 K. The considerably low calculated coefficients suggested that almost all of the C, Al, Ca, and Fe would remain in the liquid Si–Zn alloy during the silicon precipitation. As the distribution coefficients of B and P were calculated to be 0.15 and 0.26, respectively, their efficient removals were expected. Precipitation experiments were successfully performed by submerging the liquid Si–Zn alloy in molten $CaCl_2$. From the impurity analysis of the obtained silicon granules, high removal fractions were achieved for C, Al, Ca, and Fe, which were consistent with the calculated distribution coefficients. The high removal fraction of B was also confirmed when compared with the solidification from liquid silicon. Contrary to the prediction from the calculation, O was removed from the starting material of MG-Si, which was explained by the dissolution of residual oxides such as CaO into molten $CaCl_2$. The obtained silicon granules were transformed into wafers using the FZ method. For the silicon wafers, the total content of metal impurities (Al, Ca, Fe, Ti, and Zn) was less than 0.2 ppmw, wherein Al and Ca met the acceptable levels for SOG-Si. In the silicon wafers, the concentrations of P and O also decreased. In particular, the concentration of Zn decreased from 5900 ppmw in the granules to less than 0.01 ppmw in the wafers, which demonstrates the great advantage of Zn as an alloying element.

Acknowledgement

This study was partially supported by Core Research for Evolutionary Science and Technology (CREST) from the Japan Science and Technology Agency (JST); Grant-in-Aid for Scientific Research A, Grant Number 16H02410, from the Japan Society for the Promotion of Science (JSPS), the Japan Prize Foundation, the Kato Foundation for Promotion of Science, and the Joint Usage/Research Program on Zero-Emission Energy Research, Institute of Advanced Energy, Kyoto University (ZE28A12, ZE29A01).

REFERENCES

1) *Key World Energy Statistics 2019*, (IEA, Paris, 2019) p. 25.
2) *World Energy Outlook 2018*, (IEA, Paris, 2018) p. 63.
3) *Industrial Rare Metal 2019*, (Arumu Publ. Co., Tokyo, 2019) p. 19.
4) *Photovoltaic Market 2019*, (RTS Corp., Tokyo, Japan, 2019) p. 43.
5) *Trends in Photovoltaic Applications 2019*, (PVPS, IEA, Paris, 2019) p. 59.
6) H. Schweickert, K. Reusche and H. Gustsche: U.S. Patent 3011877 (1961).
7) H. Gutsche: U.S. Patent 3011877 (1962).
8) C. Bye and B. Ceccaroli: Sol. Energy Mater. Sol. Cells **130** (2014) 634–646.
9) K. Hanazawa, N. Yuge and Y. Kato: Mater. Trans. **45** (2004) 844–849.
10) G. Burns, J. Rabe and S. Yilmaz: PCT International Patent WO2005/061383 (2005).
11) K. Tang, S. Andersson, E. Nordstrand and M. Tangstad: JOM **64** (2012) 952–956.
12) X. Ma, T. Yoshikawa and K. Morita: Separ. Purif. Technol. **125** (2014) 264–268.
13) Y. Wang, X. Ma and K. Morita: Metall. Mater. Trans. B **45** (2014) 334–337.
14) S. Sakaguchi: PCT International Patent WO2007/119605 (2007).
15) T. Shimamune and I. Yoshikawa: Japanese Patent, Toku Kai H15-342016 (2003).
16) E. Robert and T. Zijlema: PCT International Patent WO2006/100114 (2006).
17) S. Honda, M. Yasueda, S. Hayashida and M. Yamaguchi: Japanese Patent, Toku Kai H19-145663 (2007).
18) T. Nohira, K. Yasuda and Y. Ito: Nat. Mater. **2** (2003) 397–401.
19) K. Yasuda, T. Nohira, K. Amezawa, Y.H. Ogata and Y. Ito: J. Electrochem. Soc. **152** (2005) D69–D74.
20) K. Yasuda, T. Nohira, R. Hagiwara and Y.H. Ogata: Electrochim. Acta **53** (2007) 106–110.
21) T. Nohira: Yoyuen Oyobi Koon Kagaku **54** (2011) 95–103 [in Japanese].
22) T. Toba, K. Yasuda, T. Nohira, X. Yang, R. Hagiwara, K. Ichitsubo, K. Masuda and T. Homma: Electrochemistry **81** (2013) 559–565.
23) X. Jin, P. Gao, D. Wang, X. Hu and G.Z. Chen: Angew. Chem. Int. Ed. **43** (2004) 733–736.
24) P.C. Pistorius and D.J. Fray: J. SAIMM **106** (2006) 31–42.
25) S. Lee, J. Hur and C. Seo: J. Ind. Eng. Chem. **14** (2008) 651–654.
26) J. Yang, S. Lu, S. Kan, X. Zhang and J. Du: Chem. Commun. (2009) 3273–3275.
27) E. Juzeliunas, A. Cox and D.J. Fray: Electrochem. Commun. **12** (2010) 1270–1274.
28) W. Xiao, X. Jin, Y. Deng, D. Wang and G.Z. Chen: J. Electroanal. Chem. **639** (2010) 130–140.
29) E. Ergül, İ. Karakaya and M. Erdoğan: J. Alloy. Compd. **509** (2011) 899–903.
30) S. Cho, F.F. Fan and A.J. Bard: Electrochim. Acta **65** (2012) 57–63.
31) H. Nishihara, T. Suzuki, H. Itoi, B. An, S. Iwamura, R. Berenguer and T. Kyotani: Nanoscale **6** (2014) 10574–10583.
32) S. Fang, H. Wang, J. Yang, S. Lu, B. Yu, J. Wang and C. Zhao: Mater. Lett. **160** (2015) 1–4.
33) S. Fang, H. Wang, J. Yang, S. Lu, B. Yu, J. Wang and C. Zhao: J. Phys. Chem. Solids **89** (2016) 1–6.
34) T. Nohira, A. Ido, T. Shimao, X. Yang, K. Yasuda, R. Hagiwara and T. Homma: ECS Trans. **75** (2016) 17–33.
35) K. Yasuda, T. Shimao, R. Hagiwara, T. Homma and T. Nohira: J. Electrochem. Soc. **164** (2017) H5049–H5056.
36) Y. Ma, A. Ido, K. Yasuda, R. Hagiwara and T. Nohira: J. Electrochem. Soc. **166** (2019) D162–D167.
37) T. Yoshikawa and K. Morita: Sci. Technol. Adv. Mater. **4** (2003) 531–537.
38) T. Yoshikawa and K. Morita: J. Cryst. Growth **311** (2009) 776–779.
39) W. Yu, W. Ma, G. Lv, Y. Ren, H. Xue and Y. Dai: Trans. Nonferrous Met. Soc. China **23** (2013) 3476–3481.
40) J. Li, Z. Guo, J. Li and L. Yu: Silicon **7** (2015) 239–246.
41) J.M. Juneja and T.K. Mukherjee: Hydrometallurgy **16** (1986) 69–75.
42) X. Ma, T. Yoshikawa and K. Morita: J. Cryst. Growth **377** (2013) 192–196.
43) S. Esfahani and M. Barati: Met. Mater. Int. **17** (2011) 823–829.
44) S. Esfahani and M. Barati: Met. Mater. Int. **17** (2011) 1009–1015.
45) T. Yoshikawa and K. Morita: Metall. Mater. Trans. B **36** (2005) 731–736.
46) T. Yoshikawa and K. Morita: J. Electrochem. Soc. **150** (2003) G465–G468.
47) Y. Chung, J.M. Toguri and R. Sridhar: Can. Metall. Quart. **40** (2001) 185–192.
48) T.B. Massalski, J.L. Murray, L.H. Bennett and H. Baker: *Binary Alloy Phase Diagrams, 2nd ed.*, (American Society for Metals, Ohio, 1986).
49) M. Haemaelaeinen and I. Isomaeki: J. Alloy. Compd. **392** (2005) 220–224.
50) M.W. Chase, Jr., C.A. Davies, J.R. Downey, Jr., D.J. Frurip, R.A. McDonald and A.N. Syverud: *JANAF Thermochemical Tables, 3rd ed.*, (American Chemical Society, Washington, DC, 1985).
51) I. Barin: *Thermochemical Data of Pure Substances, 2nd ed.*, (VCH Verlags Gesellschaft, Weinheim, 1993).
52) B. Landolt: *Thermodynamic Properties of Inorganic Materials, Part IV*, (Springer-Verlag, Berlin, 2001).
53) O. Knacke, O. Kubaschewski and K. Hesselman: *Thermochemical Properties of Inorganic Substances, 2nd ed.*, (Springer-Verlag, Berlin, 1991).
54) B. Binnewies and E. Milke: *Thermochemical Data of Elements and Compounds, 2nd ed.*, (Wiley-VCH, Weinheim, 2002).
55) M.E. Schlesinger: Chem. Rev. **102** (2002) 4267–4302.
56) I. Barin: *Thermochemical Data of Pure Substances, 3rd ed.*, (VCH Verlags Gesellschaft, Weinheim, 1995).
57) I. Barin, O. Knacke and O. Kubaschewski: *Thermochemical Properties of Inorganic Substances*, (Springer-Verlag, Berlin, 1977).
58) B.J. McBride, S. Gordon and M.A. Reno: *Thermodynamic Data for Fifty Reference Elements*, (NASA Technical Paper 3287, Ohio, 1993).
59) C. Malcolm: *NIST-JANAF Thermochemical Tables, 4th ed.*, (American Chemical Society, New York, 1998).
60) B. Landolt: *Thermodynamic Properties of Inorganic Materials, Part I*, (Springer-Verlag, Berlin, 1999).
61) P.J. Spencer, A.D. Pelton, Y. Kang, P. Chartrand and C.D. Fuerst: Calphad **32** (2008) 423–431.
62) I. Barin: *Thermochemical Data of Pure Substances, 1st ed.*, (VCH Verlags Gesellschaft, Weinheim, 1989).
63) G. Reumont, P. Perrot, J.M. Fiorani and J. Hertz: J. Phase Equilib. **21** (2000) 371–378.
64) V.S. Iorish and G.V. Belov: *On Quality of Adopted Values in Thermodynamic Databases*, (Scientific Databases Conference, Japan, 1996).
65) K. Doi, S. Ono, H. Ohtani and M. Hasebe: J. Phase Equilibria Diffus. **27** (2006) 63–74.
66) G.L. Vick and K.M. Whittle: J. Electrochem. Soc. **116** (1969) 1142–1144.
67) A.J. Bard, R. Parsons and J. Jordan: *Standard Potentials in Aqueous Solution*, (Marcel Dekker Inc., New York, 1985).
68) Z. Chen, F. Yin, M. Zhao and Z. Li: J. Phase Equilibria Diffus. **34** (2013) 366–374.
69) T. Narushima, A. Yamashita, C. Ouchi and Y. Iguchi: Mater. Trans. **43** (2002) 2120–2124.
70) H.A. Wrledt: Bull. Alloy Phase Diagrams **11** (1990) 43–61.
71) S. Otsuka and Z. Kozuka: Trans. JIM **22** (1981) 558–566.

72) R.W. Olesinski, N. Kanani and G.J. Abbaschian: Bull. Alloy Phase Diagrams **6** (1985) 130–133.
73) H. Sigmund: J. Electrochem. Soc. **129** (1982) 2809–2812.
74) E.R. Weber: Appl. Phys. A **30** (1983) 1–22.
75) S. Kuge and H. Nakashima: Jpn. J. Appl. Phys. **30** (1991) 2659–2663.
76) H. Okamoto: J. Phase Equilibria Diffus. **29** (2008) 211–212.
77) F.A. Trumbore: Bell Syst. Tech. J. **39** (1960) 205–233.
78) T. Yoshikawa and K. Morita: Sci. Technol. Adv. Mater. **4** (2003) 531–537.
79) T.R. Hogness: J. Am. Chem. Soc. **43** (1921) 1621–1628.
80) K.C. Mills and L. Courtney: ISIJ Int. **40** (2000) S130–S138.
81) V.P. Popov and B.R. Pamplin: J. Cryst. Growth **15** (1972) 129–132.
82) A. Miller, R.G. Humphreys and B. Chapman: J. Phys. Colloques **36** (1975) C3-31–C3-34.
83) T. Ohmi and T. Nitta (eds.): *Silicon no Kagaku, 1st ed.*, (Realize Inc., Tokyo, 1996) p. 1017 [in Japanese].
84) M.W. Chase, Jr., C.A. Davies, J.R. Downey, Jr., D.J. Frurip, R.A. McDonald and A.N. Syverud: *NIST–JANAF Thermochemical Tables, 4th ed.*, (American Chemical Society, Washington, DC, 1998).
85) T. Yoshikawa and K. Morita: ISIJ Int. **45** (2005) 967–971.
86) F.A. Trumbore: Bell Syst. Tech. J. **39** (1960) 205–233.